5.1. Introduction

Low dimensional materials have attracted considerable attention recently because of their suitability from the application point of view. Dimensional confinement initiates enormous modification in the physical and chemical properties of the material. Enlargement of the surface-to-volume ratio enhances the pertinence of the material in various fields featuring intriguing properties. Owing to strain and stress inception at the interface of a confined system, thermally generated lattice distortion commences and results in electron-phonon, phonon-phonon, or spin-phonon interactions [83]. These phenomena inaugurate specific transitions, alignments or distortions in transport properties of materials deviating from the conventional bulk mechanisms. Such interactions can be probed and described by a non-contact method of Raman line shift. By Raman spectroscopy, the anharmonic behavior of phonons in the lower dimensional materials can be investigated under the variation of temperatures.

2-D topological insulators (TIs) demonstrate enhanced surface properties as compared to the bulk states of quantum matter having attractive gap-less metallic surface states, which are protected with Time-Reversal Symmetry (TRS) [4], [118], [141]. The inter-atomic distance inside the materials can be reduced by imposing external pressure, which affects the material property enormously. However, specific simulations are required to understand the interfaces and the gap structure to transmit the gap minimum in the crystalline lattice. In Bi_2Te_3 thin film on top of the iron-based ferromagnets $FeTe_{0.55}Se_{0.45}$, the proximity effect was induced. A clear indication of a two-fold symmetry of the order parameter was detected, and a lengthened vortex structure was recognized, accompanying this effect [151]. Iron chalcogenide FeSe has a tetragonal phase with PbO-type structure and a hexagonal phase with NiAs-type structure [188], exhibiting structural transformation

by modifying the atomic ratio of Fe and Se. Such FeSe type chalcogenide material possesses potential applications as spin injection materials in spintronics [152]. This attributes ferromagnetic (FM) property at around room temperature. A thin layer of such magnetic tetragonal structure might be a potential source of spin injection into a conventional TI having intrinsic spin momentum locking. Thus, the edge state of a di-chalcogenide type TI, Sb_2Te_3 can evolve with enormous modifications by emerging thin layers of FeSe over it. The inter-layer proximity is a matter of attraction, as it provides an interface between tetragonal FeSe and rhombohedral Sb_2Te_3. Interestingly, such a structural anomaly may induce a coupling between different charge carriers with phonon initiated by lattice vibration and distortion at the interface. Also, such FM/TI/FM heterostructures may exhibit certain magnetic ordering at room temperature initiated by the ferromagnetic FeSe layers at the interfaces of the system enhancing the applicability of the system as next generation low energy spintronics devices, high storage memory devices and faster quantum computation.

We prepared the heterostructures of FeSe/Sb_2Te_3/FeSe, using the thickness calibration procedure discussed in section 2.2.3, where we varied the number of shots modifying the thickness of each layer. The thickness and number of shots corresponding to each layer of prepared heterostructures are listed in Table 5.1. Interestingly, only the heterostructure of 75.3 nm thickness shows a significant anomaly in its Magnetization value at the vicinity of 475 K temperature, whereas the thicker heterostructures exhibited usual Magnetization curves with temperature variation, which is described elaborately in the section 5.2. This observation exemplifies the dominancy of the interfacial local spin evolution in the 75.3 nm system, over the intrinsic bulk magnetization at a particular temperature range which is discussed later in this article. Further, in this particular system,

we have measured the physical and magnetic properties along with the Raman spectra evidencing the phenomena behind such behavior.

Table 5.1: The thicknesses of the prepared heterostructures are listed with the number of shots.

	FeSe	Sb_2Te_3	FeSe	Total
75.3 nm				
Number of Shots	200	500	200	900
Expected thickness (nm)	15	50	15	80
Measured thickness (nm)				75.3
91.9 nm				
Number of Shots	400	500	400	1300
Expected thickness (nm)	20	50	20	90
Measured thickness (nm)				91.9
271.8 nm				
Number of Shots	1400	1500	1400	4300
Expected thickness (nm)	60	165	60	285
Measured thickness (nm)				271.8
428.8 nm				
Number of Shots	2500	2000	25000	7000
Expected thickness (nm)	100	200	100	400
Measured thickness (nm)				428.8

5.2 Comparing Magnetic Properties of As-prepared Heterostructures

We measured the magnetic moments for all the prepared heterostructures of different thicknesses concerning temperature from 300 to 700 K. The value of magnetic moment differs with varying thicknesses as shown in Figure 5.1. All samples show usual magnetization with temperature. However, it was surprising to observe that, the heterostructure with 75.3 nm thickness attributes an unusual magnetic anomaly in the temperature range 465 K to 485 K in both ZFC/FC magnetization curves, and compared

with other heterostructure in Figure 5.1 here. This dip in magnetization was described as a certain local spin ordering in the vicinity of the interface of FeSe and Sb_2Te_3 that appeared due to lattice distortion and phonon vibrations at high temperatures. Besides this, the charge order driven local spin ordering might also be a reason behind such anomaly in M-T curves in the vicinity of 475 K (T_{sp}) temperature will be discussed briefly in result and discussions section. Thus, it can be understood unambiguously that there is some short-range local magnetic ordering in the 75.3 nm system around 475 K. But increasing the thickness, the up written drop disappeared indicating that there is no local ordering in those systems. The enhancement of thickness directly corresponds to the increasing bulk behavior in the system. For 91.9 nm, 271.8 nm, and 428.8 nm heterostructures, the intrinsic bulk effect dominates over the interfacial proximity effect diminishing the probability of proximity induced local spin ordering. Further, in the 75.3 nm film, spin-phonon coupling initiated by local charge ordering at the proximity of the interface in the prepared heterostructure was confirmed using the Raman spectroscopy study. We measured moment vs. magnetic field for all the heterostructures at 350 K and 580 K, which signifies the similar ferromagnetic behavior as shown in Figure 5.2 (a-d). The change in saturation magnetization is larger for the 75.3 nm thick sample as compared to others might be due to the presence of local spin ordering in-between. Thus, we have measured the magnetic properties of the heterostructures with different thicknesses. But we observed local magnetic ordering only in the 75.3 nm heterostructure, so we measured the Raman spectra and transport properties only for this system to understand the phenomena behind such behavior. After all observations, we concluded that due to the dominancy of the interfacial states in the 75.3 nm system, local spin evolution was dominated over the intrinsic bulk magnetization, and this local spin evolution initiated a short-range ordering as shown in Figure 5.1.

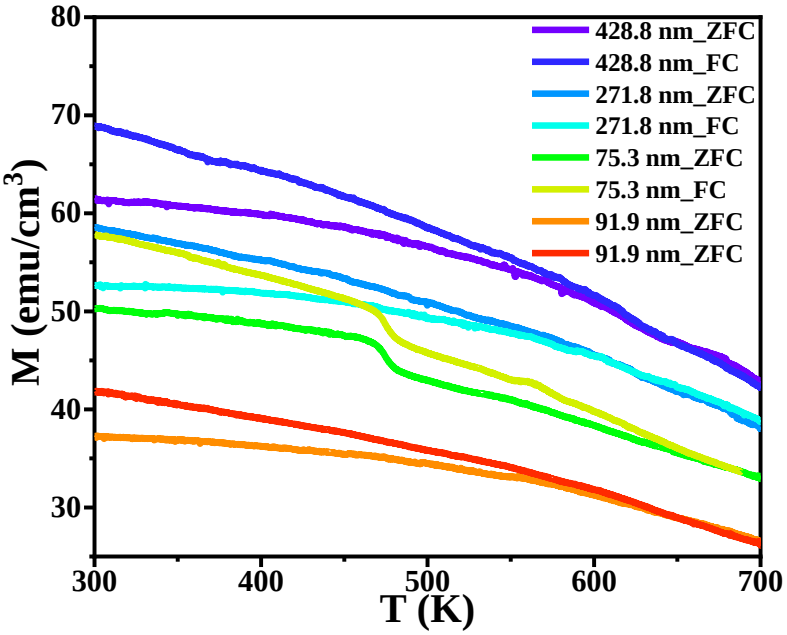

Figure 5.1: The magnetic moment vs. temperature for the heterostructures of different thicknesses.

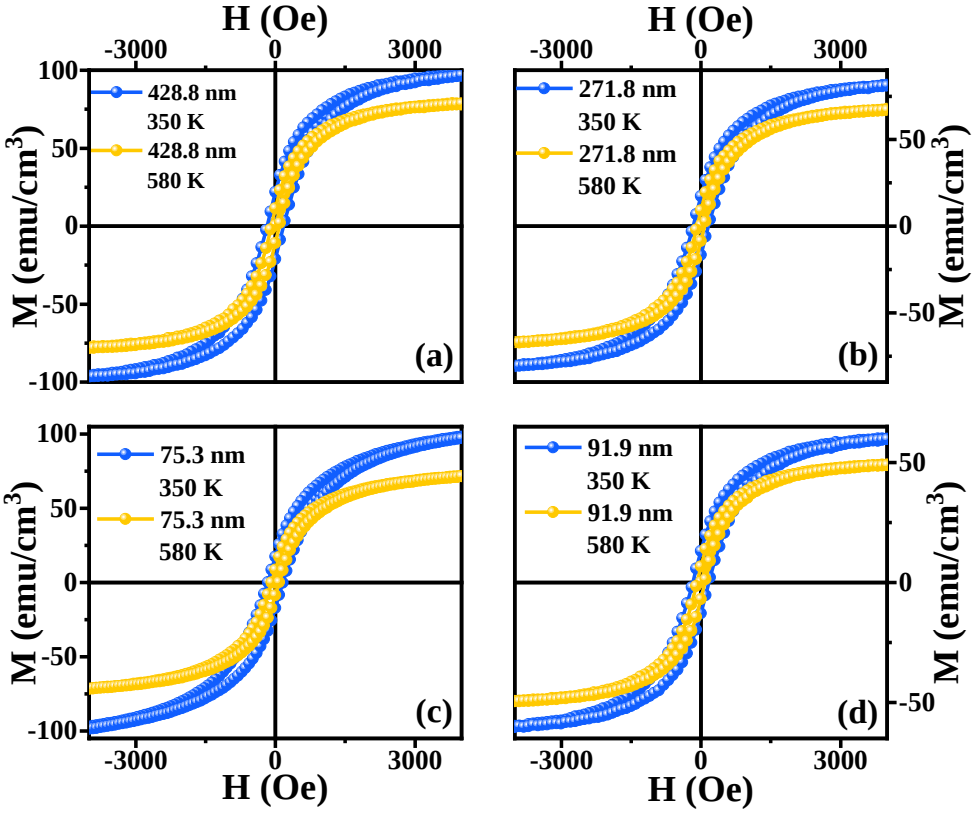

Figure 5.2: Magnetic moment variation with magnetic field for the heterostructures of thicknesses (a) 428.8 nm, (b) 271.8 nm, (c) 75.3 nm, (d) 91.9 nm.

5.3 Results and Discussion

5.3.1 Structural and Morphological Analysis

5.3.1.1 Structural Confirmation

We have discussed the structural, morphological, physical and magnetic properties of FeSe/Sb_2Te_3/FeSe heterostructure of thickness ~75.3 nm in this chapter. X-ray diffraction was done with the grazing incidence (GI) angle was fixed at 0.2°. At such a low GI angle, the penetration depth remains exceptionally shallow, and thus the penetrated X-rays propagate almost parallel to the film surface and come out by diffraction from the lattice planes. In this way, an out-of-plane X-Ray Diffraction (XRD) scan provides structural information on thin films by nullifying the substrate effect. Thus, sometimes the diffraction peak signal becomes very weak compared to the background signal and appears to be unclear due to low thickness. For our case, the FeSe layer thickness is much less (~15 nm) as compared to the Sb_2Te_3 layer (~50 nm). So, the peaks corresponding to FeSe did not appear well in the diffraction pattern. Thus, to confirm the structural information, we studied the diffraction pattern for the heterostructures of larger thicknesses and compared them with the diffraction peaks corresponding to Sb_2Te_3 and FeSe targets as shown in the Figure 5.3. The diffraction peaks are more significant for higher thicknesses as expected. For the 428.8 nm thick heterostructure all the peak positions corresponding to FeSe and Sb_2Te_3 are visible as shown in the inset of Figure 5.3.

The crystalline nature of the prepared 75.3 nm thick FeSe/Sb_2Te_3/FeSe heterostructure was confirmed by performing out-of-plane X-ray Diffraction measurement by keeping the scattering vector perpendicular to the film plane. Diffraction maxima corresponding to (001) plane of Sb_2Te_3 was established along with (001), (101) and (112) peaks of FeSe tetragonal phase (Figure 5.4(a)). The integrated peak width at half maximum

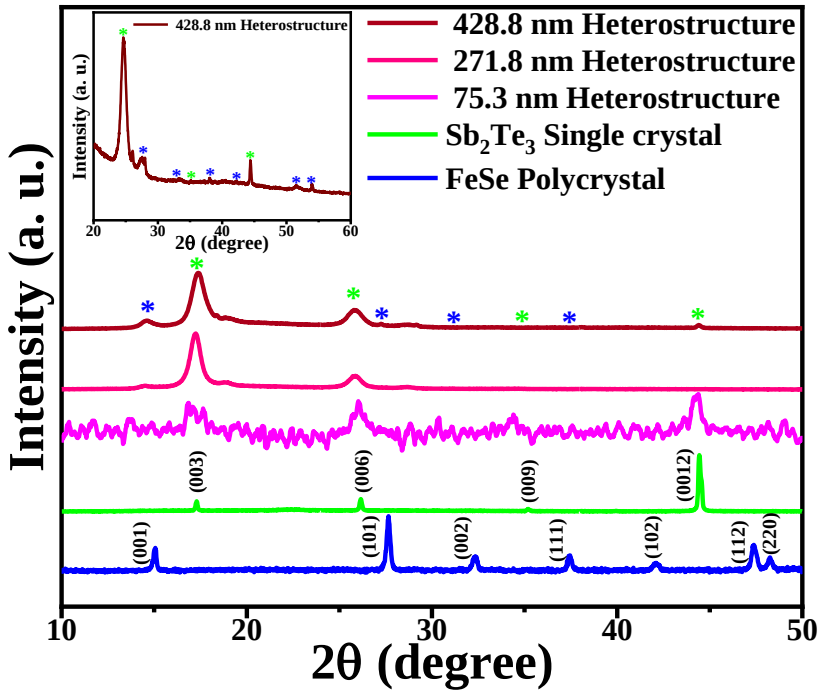

Figure 5.3: The X-Ray Diffraction patterns of as-prepared heterostructures compared with Sb_2Te_3 single crystal and FeSe polycrystal. Inset shows a closer view of the 428.8 nm thick heterostructure.

(β) was determined to be 0.69851 and 0.71752, corresponding to (006) and (0012) planes of Sb_2Te_3 based heterostructure. As the (006) and (0012) peaks are the most intense ones, they will give a statistically more accurate value of average crystallite size. Thus, the average crystallite size (D) was calculated using the Debye-Scherrer formula [189], $D = K\lambda/\beta COS\theta$, where K is the shape factor which is taken as 0.9 depending on the assumptions made in theory and λ is the radiation wavelength (1.5409 Å). The average value of crystallite size was determined as 11.81 nm which is nearly five times smaller as compared to the bulk value (51.45 nm). As the Scherrer formula neglects the strain effect, and we didn't get multiple diffraction peaks, we were unable to decouple the strain and size broadening. However, the finite grain size adds Gaussian nature into the Lorentzian diffraction peak shape, which is the first effect of dimensional confinement while preparing thin films from the single crystalline 3-D bulk structure. However, due to lower thickness, the diffraction peak signal became very weak compared to the background signal and

appeared to be unclear in Figure 5.4(a). Thus, to confirm the structural information, we studied the diffraction pattern for the heterostructures of larger thicknesses and compared them with the diffraction peaks corresponding to Sb_2Te_3 and FeSe targets as shown in Figure 5.3. The diffraction peaks appeared to be more significant for higher thicknesses as expected.

5.3.1.2 Morphological Analysis

The heterostructure was allowed to grow on the substrate along the (00*l*) direction. However, during thin film growth, due to lattice parameter mismatch, there will be the inception of lattice strain [83], which is discussed in the 'Film fabrication' section (2.2.3.1) briefly. These microstructural defects will mediate to the surface, and therefore to study the evolution of surface texture after film growth, AFM measurement was carried out in inter-mediated contact mode. The average roughness was calculated (using NOVA_PX software) to be 5.768 nm corresponding to the surface topography of 75.3 nm thick FeSe/Sb_2Te_3/FeSe heterostructure, as shown in Figure 5.4(b). As AFM analyses a large number of data points (512×512), thus to get a proper picture of the topography, a standard statistical approach has been used to calculate all the other height shape parameters and they are listed in Table 5.2. The +ve skewness value confirms the predominance of peaks in the surface topography which are leptokurtic in nature as the Kurtosis value is greater than three. As discussed in section 2.2.3, due to lattice mismatch, surface roughness starts increasing above a critical thickness for each sample, and also it is highly likely during heterostructure formation. Moreover, when the accumulated strain energy in the films is released, it triggers island formation (sometimes a large one) [83]. It has also been observed in our case that very few islands over the film surface, but they are not hindering the overall transport and magnetic properties of the sample. The top surface morphology exhibits

vibrant pyramid-shaped characteristic triangular islands. Such surface profile is strong evidence of the Stranski-Krastanov (S-K) type growth [80] in the layer-by-layer deposition [190] of Sb_2Te_3 and FeSe on the Si (001) substrate. In order to understand the surface profile and grain size of the prepared FeSe/Sb_2Te_3/FeSe heterostructures, SEM images were taken (Figure 5.4 (c)). EDX measurement confirmed the presence of every element in the prepared film. No extra elements like C or O were observed, indicating the high purity of the samples (Figure 5.4(d)). The atomic percentage measured by EDX spectra justifies that the FeSe layer is much thinner than the Sb_2Te_3 layer. The well-distributed hexagonal grains also confirm the single orientational growth of the film. The grain size was calculated in the order of 300 to 400 nm.

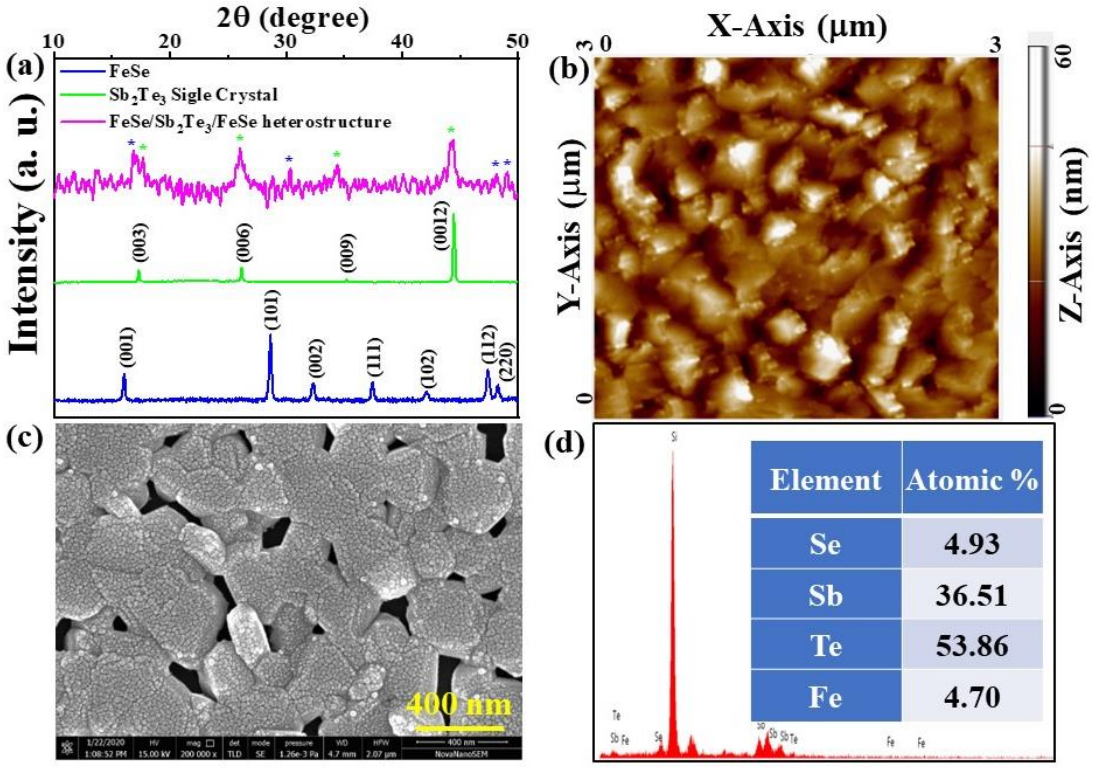

Figure 5.4: (a) X-Ray Diffraction spectra of the prepared 75.3 nm thick FeSe/Sb_2Te_3/FeSe heterostructures associated with the polycrystalline tetragonal structure of FeSe and single-crystalline rhombohedral structure of Sb_2Te_3, (b) AFM morphology with the height profile, (c) FESEM image of the 75.3 nm FeSe/Sb_2Te_3/FeSe surface showing the grain distribution, (d) EDX spectra of FeSe/Sb_2Te_3/FeSe showing atomic profile.

Table 5.2: Statistical parameters assessed from AFM measurement.

Height parameters from AFM	**FS/ST/FS**
Root mean square roughness	7.472 nm
Average roughness	5.768 nm
Shape parameters	
Kurtosis	3.636
Skewness	0.274

5.3.2 Transport Property

To investigate the transport properties of the layered system, longitudinal resistivity was measured. Figure 5.5(a) is displaying the striking behavior with varying temperatures from 2 K to 300 K for the heterostructure. In this figure, it has been observed that from room temperature, resistivity increases with the decreasing temperature down to 150 K and shows a broad hump adjacent to 150 K. Subsequently, lowering the temperature, resistivity shows metallic behavior down to 15 K and then again starts increasing. The increment in resistivity with reducing temperature with T^{-1} dependency from room temperature might be initiated by coulomb drag contributed by plasmon. The broad transition near 150 K might be associated with plasmon-polaron formation [173]–[175]. The Resistivity varies linearly with temperature between 20 to 60 K. Below 15 K, resistance displays a specific feature corresponding to the Kondo effect (Figure 5.5(b)), where the R-T data of the heterostructure was fitted using an abridged Kondo model given by [172], [178], [191],

$$R(T) = R_o + qT^2 + pT^5 + R_k\left(\frac{T}{T_k}\right) \tag{5.1}$$

where R_o signifies the residual resistance occurred by atomic disorder in the system. The T^2 and T^5 terms imply the electron-electron and electron-phonon interactions respectively. The characterizing parameters were estimated using the equation [172], [178], [191],

$$R_k\left(\frac{T}{T_k}\right) = R_k(T=0)\left[\frac{T_k'^2}{T^2+T_k'^2}\right]^S \quad (5.2)$$

where $T_k' = T_k/\left(2^{1/S}-1\right)^{1/2}$ and S was secured to 0.225. All the evaluated parameters from the Kondo model fitting shown in Figure 5.5(b) have been listed in Table 5.3. The Kondo temperature was found to be around 5.4 K for this particular system. The Kondo model positively describes the scattering of electrons in a metallic system in the presence of magnetic impurities and results in a characteristic change in the resistivity. Thus, there is a possibility of the existence of certain magnetic ordering in the above-described system. Thus, the observed growth in the resistivity value below 15 K might be a result of the gap

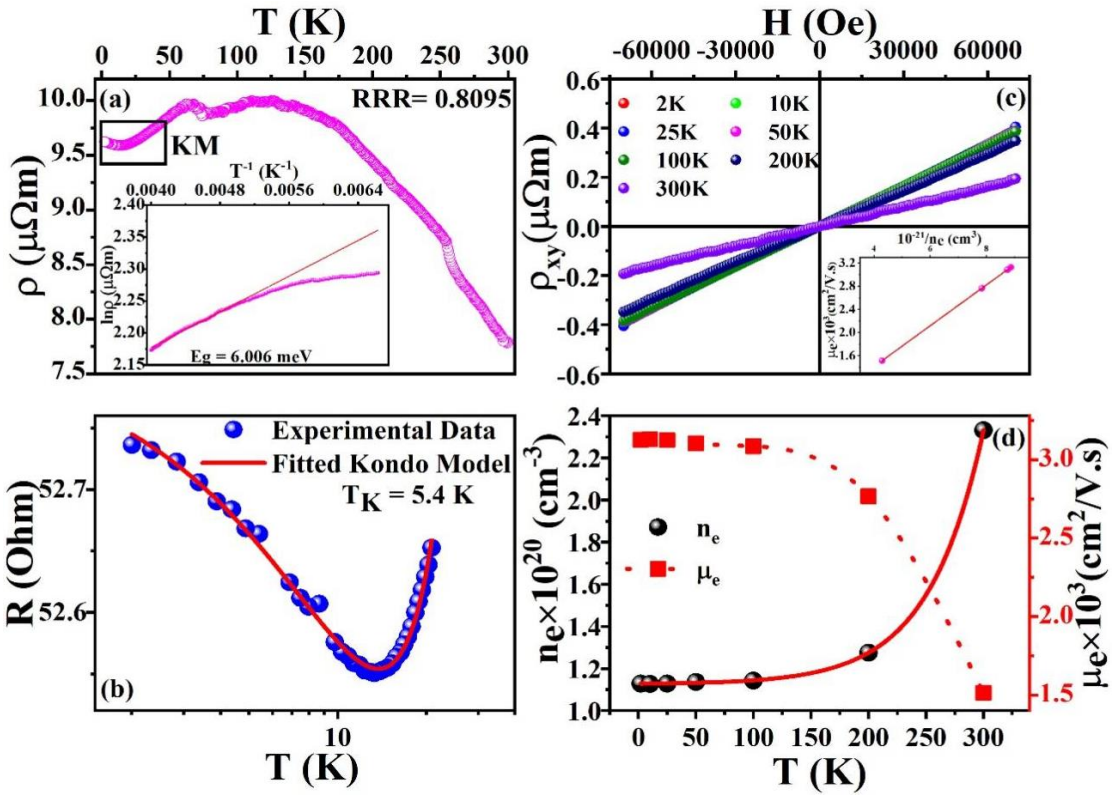

Figure 5.5: (a) Resistivity variation with temperature ranging from 2 to 300 K. Inset shows Logarithmic plot of resistivity with the inverse of temperature equipped with Arrhenius law, (b) The resistance varying temperature fitted with Kondo model, (c) Hall resistivity variation with the magnetic field at different temperatures. The bottom corner inset attributes the dependence of linear mobility on charge carrier density, (d) The temperature dependency of mobility and charge carrier density fitted by double exponential decay.

Table 5.3 Resistance was fitted with the Kondo model below 15 K temperature and the evaluated parameters are listed here.

Kondo Parameters	**FS/ST/FS**
R_0	52.81 Ω
q (e-e interaction)	$1.13\times10^{-3}\ \Omega/K^2$
p (e-p interaction)	$2.17761\times10^{-8}\ \Omega/K^5$
T_K (Kondo temperature)	5.44 K

opening at the Dirac point [192]. Further, the Residual Resistance Ratio (RRR) was calculated as 0.8095. The activation energy was determined using the relation $\rho = Aexp(E_g/2K_BT)$, where K_B is the Boltzmann constant. Activation energy was evaluated as 6.006 meV from the linearly fitted lnρ *vs.* 1/T curve (shown in the inset of Figure 5.5(a)) in the semiconducting region.

The isothermal transverse resistivity, which is commonly known as Hall resistivity (ρ_{xy}), was measured with varying magnetic field (H) from -7 to +7 T at different temperatures (Figure 5.5(c)). This transverse resistivity data shows a positive slope with H, which strongly recommends that the p-type charge carriers are dominating in our system [42], [172]. The estimated values of carrier concentration (n_e) and carrier mobility (μ_e) from Hall resistivity data at different temperatures are presented in the top corner insets of Figure 5.5(c). The charge carrier concentration n_e was nearly constant below 100 K and increased from 1.14285×10^{20} to 2.33181×10^{20} (at 300 K), followed by double exponential Arrhenius law with T^{-1} as [193],

$$n_e = n_0 + n_1 e^{-\frac{E_{g_1}}{K_B T}} + n_2 e^{-\frac{E_{g_2}}{K_B T}} \quad (5.3)$$

Here, E_{g_1} and E_{g_2} were evaluated as 115.59 meV and 5.58 meV, respectively, for the present system. The estimated value of E_{g_2} is comparable to the electrical bandgap of Sb_2Te_3 [194],

[195]. But, the value of E_{g_1} is significantly less with respect to the electronic binding energy of the system which can be classified as the activation energy of the system. This value of activation energy is comparable to the value evaluated from the linearly fitted lnρ *vs.* 1/T curve (Figure 5.5(b)). Further, μ_e *vs.* $1/n_e$ was fitted linearly with a slope of 3.527×10^{23}, which is shown in the bottom inset of Figure 5.5(c). Such a small value of thermal activation energy is associated with the semiconductor-like behavior, which has been observed earlier above 150 K (which can be seen in Figure 5.5(a)). The enhanced charge carrier mobility with T^{-1} is the probable reason behind the metallic behavior below 150 K. Interestingly, the temperature independence of the charge carrier density below 100 K is consistent with the magneto-resistance data presented in Figure 5.6(a). The linear region of the MR data at a higher magnetic field can be explained in terms of n_e [35].

Table 5.4 Arrhenius law fitted parameters over charge carrier density calculated from hall resistivity.

Evaluated parameters from Hall resistivity	**FS/ST/FS**
n_0	1.12732×10^{20} cm^{-3}
n_1	2.99612×10^{18} cm^{-3}
Eg_1	5.5847894×10^{-3} eV
n_2	1.0322410^{22} cm^{-3}
Eg_2	115.5866×10^{-3} Ev

Moreover, we have measured the longitudinal resistivity (ρ_{xx}) and the magneto-resistance which was defined as MR% = $\{\rho_{xx}(H) - \rho_{xx}(0)/\rho_{xx}(0)\}$, where $\rho_{xx}(H)$ is the field modulated resistivity value, and $\rho_{xx}(0)$ corresponds to the resistivity without the application of magnetic field. The MR% demonstrates linear reliance on magnetic field (H) up to 50 K, whereas, it exhibits parabolic nature at higher temperature. Thus, the MR% shows quadratic dependency with H (Figure 5.6(c)) above 50 K, for the present heterostructure. The linear dependency of MR% on the magnetic field below 50 K, suggests

the presence of weak anti-localization (WAL) below 50 K. The gradual transformation of MR% from linear to parabolic nature arises owing to the suppression of WAL phenomena and domination of the weak localization (WL). Consequently, to comprehend the crossover from WAL to WL phenomena and the consequence of topological surface states (TSS), the Hikami-Larkin-Nagaoka (HLN) formula was fitted on magneto-conductivity (MC) data as [145],

$$\Delta\sigma = \sigma(H) - \sigma(0) = A\left[\psi\left(\frac{1}{2} + \frac{h}{8\pi eBl_{\varphi}^{2}}\right) - ln\left(\frac{h}{8\pi eBl_{\varphi}^{2}}\right)\right] \quad (5.4)$$

where, $A = \alpha e^2/\pi h$ epitomizes the number of conduction channels that exist in the system with $\alpha = -1/2$ per conduction channel, ψ signifies digamma function, l_{φ} represents the phase coherence length. Figure 5.6(b) is showing the HLN fitting of MC data below 50 K, up to 1T magnetic field. The obtained values of l_{φ} at different temperatures from this fitting are shown in Table 5.5. However, at higher temperatures (above 50 K) HLN formula does not fit properly with the MC data due to the reduction in WAL and enrichment in WL. The MR data shows linear behavior above 4 T throughout the measured temperature range, which is shown in the right inset of Figure 5.6(d). Slope *s* was determined from the linearly fitted MR *vs*. H data in the range of 4 T to 7 T [196]. This *s* has a linear dependency with temperature (left inset of Figure 5.6(d)) and square root dependency with n_e (Figure 5.6(d)). Therefore, from the estimated value of s and n_e in the present system, it can be concluded that the longitudinal resistivity (ρ_{xx}) and the transverse resistivity (ρ_{xy}) are related to each other as, $\rho_{xx}/\rho_{xy} = {n_e}^{3/2}$.

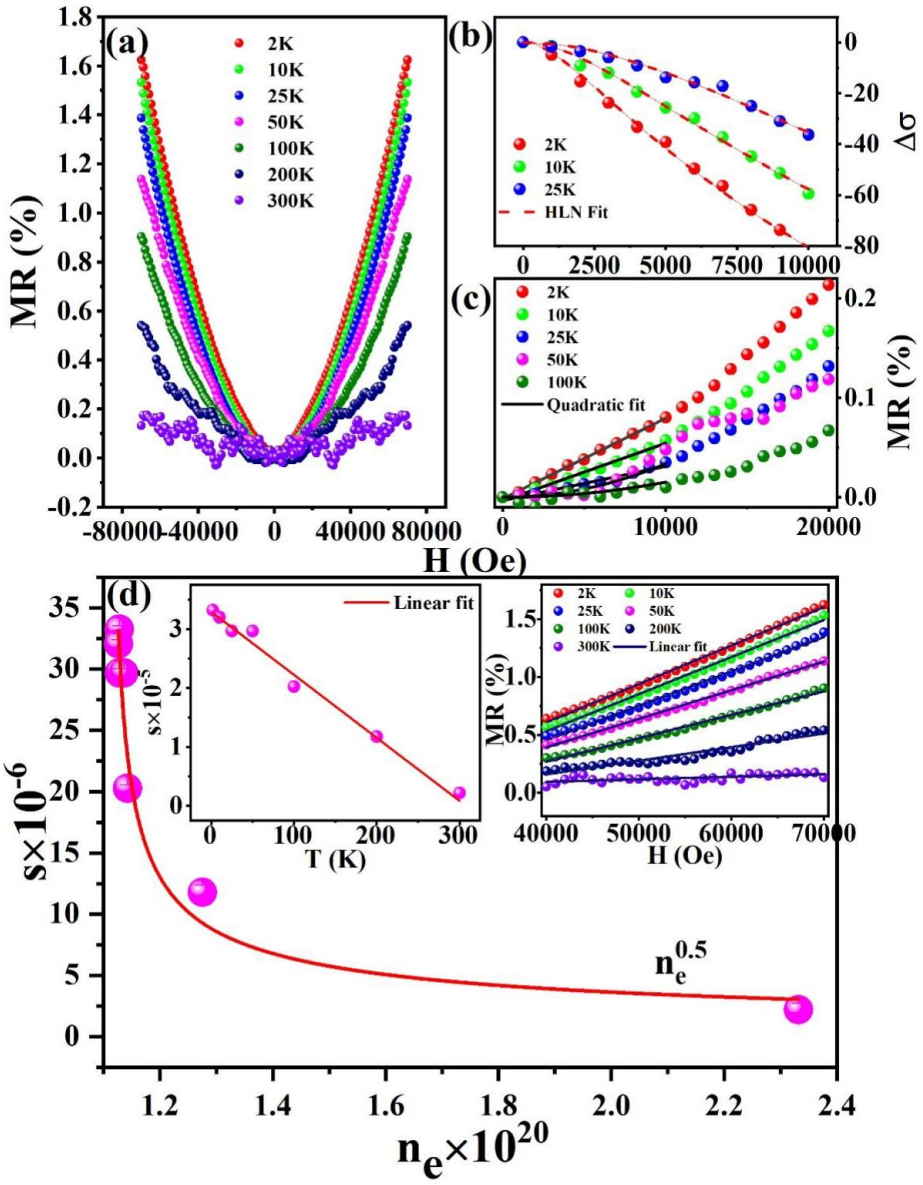

Figure 5.6: (a) MR% with magnetic field variation at a temperature ranging from 2 to 300 K, (b) HLN fitted conductivity plot, (c) Magnetic field dependency of MR%. (d) The slope of the linear fitted MR plotted with charge carrier density. The left inset shows the temperature dependency of the slope and the linearly fitted MR% data at above 4 T magnetic field is shown in the right inset.

Table 5.5 Phase coherence length at different temperatures premeditated using HLN fitting.

T	**Lφ**
2	1.33×10^{-11}
10	7.486×10^{-12}
25	3.3015×10^{-12}

5.3.3 Magnetic Property

Magnetic properties were measured at a low-temperature range to investigate an inevitable rise in resistivity at low temperature (below 15 K), which was fitted with the Kondo model (Figure 5.5(a) inset). Magnetization (M) was measured at 5 K with the varying magnetic field (H) displaying distinct antiferromagnetic ordering (Figure 5.7(a)). Such anti-parallel magnetic arrangement at low temperature has been examined in Sb_2Te_3 single-crystalline TI in the presence of different magnetic transition metal ions [170], [171]. Existing iron ions of the FeSe layers might be introducing the spins at the interfaces of the present heterostructure, which eventually modifies the spin orientation in Sb_2Te_3. However, at higher temperatures, parallel spin ordering starts dominating over the anti-parallel ordering. The presence of a tetragonal FeSe layer, which exhibits long-range ferromagnetic order ranging from moderate to higher temperature [168], [169], might be a reason behind such an interesting magnetic arrangement. This phenomenon was evidenced by the M-H measurement at 50 K (Figure 5.7(b)), which manifests the presence of both parallel and anti-parallel spins at this temperature range. Further, with rising the temperature a complete ferromagnetic ordering was experienced in the system. Figure 5.7(c) demonstrates well-defined ferromagnetic M-H loops at 350 K and 580 K. The long-range ferromagnetic ordering was evaluated by subtracting the diamagnetic contribution from the measured data. The value of Magnetization decreases with raising the temperature due to randomization of spins owing to high thermal energy. At 350 K and 580 K, the saturation Magnetization (M_s) was achieved at 100 and 70 emu/cm^3, respectively. The M-H hysteresis diminishes with increasing temperature beyond 350 K. Temperature dependency of Magnetization (M-T) was recorded at zero-field cooling (ZFC) and field cooling (FC) conditions applying 10^3 Oe magnetic field (H_{app}) in the temperature region 5 K to 700 K (Figure 5.7(d)). The M-T measurement demonstrates a transition at 22 K (T_1), which is

supported with the reversed resistance curve below 15 K, followed by the Kondo model. Near the Kondo temperature (5.4 K), antiferromagnetic ordering was confirmed by perceiving the M-H statistics at 5 K (Figure 5.7(a)). This is consistent with the increase in resistivity value below 15 K due to the manifestation of anti-parallel spin alignment at the interface of the layered system, as has been discussed earlier. The Magnetization displays a broad hump at a wide range of temperatures around 300 K, which is related to the reorientation of anti-parallel to parallel spin ordering, that has also been probed using M(H) curves. Further, FC and ZFC M-T curves merged at 680 K (T_2), suggesting a paramagnetic transition. Additionally, both ZFC and FC Magnetization show a certain continuous drop from 465 K to 485 K which is demonstrated as a shaded region in the inset of Figure 5.7(d). Such a dip in Magnetization signifies certain local spin ordering in the vicinity of the interface of FeSe and Sb_2Te_3. The above-mentioned anomaly in the Magnetization curve is disappeared with increasing the thickness of the heterostructure (shown in Figure 5.1), indicating the increasing intrinsic bulk behavior in the system dominates over the interfacial proximity effect diminishing the probability of proximity induced local spin ordering. Further, due to the observed anomaly in Magnetization of the 75.3 nm film, we have carried out a detailed Raman study to elaborate the effect of local charge ordering at the proximity of the interface for this particular heterostructure. Here, we would like to mention that the tetragonal FeSe is ferromagnetic [197], [198] above room temperature whereas Sb_2Te_3 is nonmagnetic [170], [171], [199], [200]. However, the above-mentioned local spin ordering may appear owing to lattice distortion and phonon vibrations at high temperatures. Other than this, the charge order driven local spin ordering also might be a reason behind such anomaly in M-T curves in the vicinity of 475 K (T_{sp}). Thus, there is some short-range local magnetic ordering in the system around 475 K.

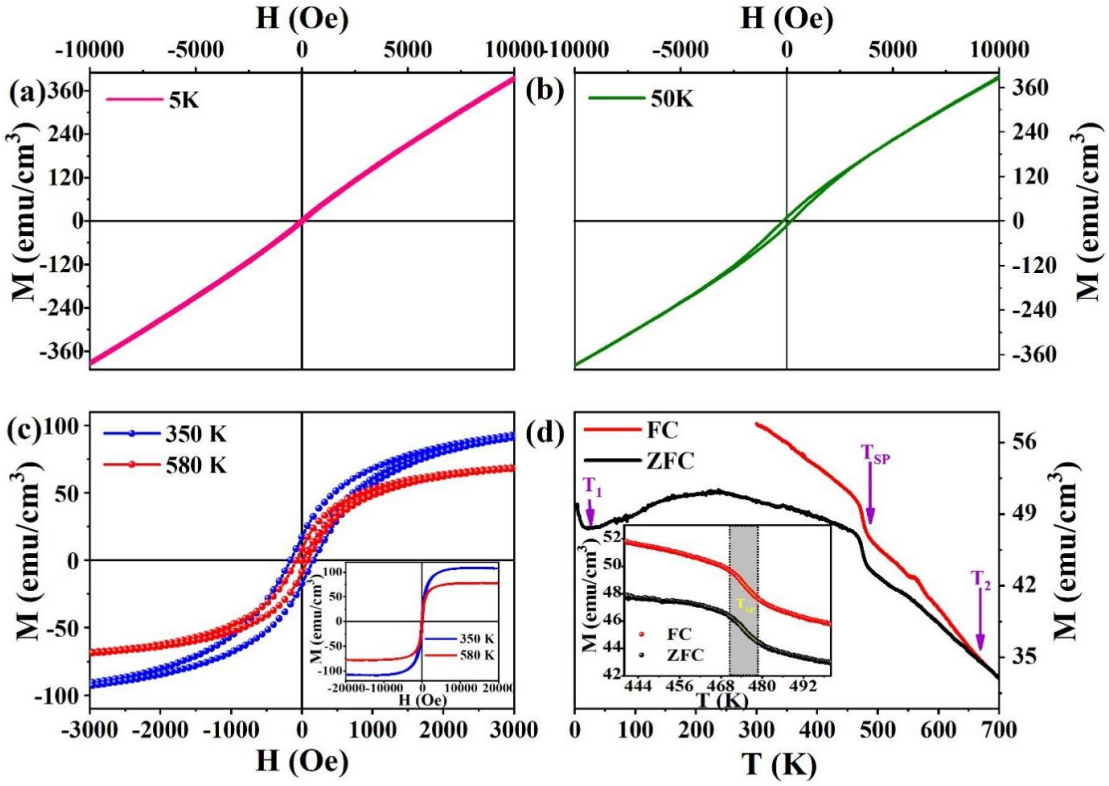

Figure 5.7: (a) M-H measured at 5 K temperature. (b) M-H measured at 50 K temperature. (c) M-H loop at 350 K and 580 K temperatures from -3000 to 3000 Oe. Inset illustrates the entire range of the M-H loop at 350 K and 580 K temperatures. (d) M-T plot at ZFC and FC condition from 5 to 700 K. Inset shows the M-T curve for enlarged ZFC and FC showing the transition around 475 K (shaded region).

5.3.4 Raman Study

Raman spectroscopy is an important tool for detecting any local/global phase (viz., structural, magnetic or electrical) transitions, owing to certain modifications in vibrational modes around the transition temperatures. A recent study has been carried out by *Ke Wang et al.*[201] for 2-D magnet CrI_3 providing fundamental information about the spin-lattice coupling. A similar relationship between the phononic properties and magnetic ordering in the confined system has been described in the present report [201], [202]. Pure Sb_2Te_3 contains five atoms in a respective primitive unit cell as covalently bonded piles of Te(1)–Sb–Te(2)–Sb–Te(1), which are secured by weak van der Wall force creating each quintuple layer. This inter-planer force can also modify the corresponding Raman or infrared active phonon frequencies. Such cell contains fifteen lattice-driven modes, three among them are

acoustical modes, and the rest twelve are optical modes. As reported by the Group theory, at ambient conditions, those optical phonon modes are distinguished as $2A_{1g}$, $2E_g$, $3A_{1u}$, and $3E_u$ at the Γ point [203]. Among them, A_{1g} and E_g modes are Raman active. Raman active modes are nomenclatured as transverse optical phonon modes (TO) and the infrared active modes which are denoted as longitudinal optical phonons (LO) considering the direction of vibration from the Brillouin Zone (BZ) center. Raman and infrared active modes are mutually exclusive by crystal inversion symmetry. To probe, if any spectacular modification of Raman modes occurs in our system, the Raman spectra have been collected over a wide temperature range from 100 K to 550 K by exciting the sample with a 633 nm laser, which is shown in Figure 5.8(a). In this spectrum, we have observed the vibration modes centered around 68.36, 92.06, 121.50, 140.00 and 166.50 cm^{-1} at room temperature (Figure 5.8(a)). The Raman line shifts centered around 68.36, 121.50 and 166.50 cm^{-1} are distinguished as A_{1g}^1, E_g^2 and A_{1g}^2 modes [204]–[206], respectively. The lowest energy mode, E_g^1 is not visible in the spectra, which might be due to the intensified Rayleigh background owing to the enhancement of elastic scattering for the confinement along the c axis of the film. However, the Raman shift centered around 92.06 and 140.00 cm^{-1} correspond to infrared active E_u^2 and A_{2u}^3 modes respectively [206]. There is also a possibility of arising these modes (i. e. the modes centered around 92.06 and 140.00 cm^{-1}) initiated by the atomic vibration in Te atoms [207] in the rhombohedral structure of Sb_2Te_3 and can be denoted as E^1 and E^2 respectively. Such vibration may occur due to the inter-layer proximity effect at the junction of the tetragonal structure of iron chalcogenide and rhombohedral di-chalcogenide Sb_2Te_3. Te-based chalcogenides show such vibrational phonon modes in the tetragonal Te atoms [207], [208] and these modes can be TO or LO types depending on the crystal structure and the direction of vibration. Here, it can also be mentioned that the present heterostructure is confined along the c axis (less than 100 nm

thick), thus there is a possibility of breaking the translational symmetry. Such crystal symmetry breaking gives rise to the infrared active LO modes in the Raman spectra. Therefore, it can be unambiguously understood that the observed E_u^2+E^1 and A_{2u}^3+E^2 vibration modes are infrared active. In this investigation, we have denoted the Raman shift at 92.06 cm^{-1} as E'(Te) and shift at 140 cm^{-1} as E''(Te). Apart from the Raman modes mentioned earlier, an infrared active A_{2u}^2 mode was examined at 113.64 cm^{-1} at 100 K. This Raman shift might be corresponding to the A^1 vibration mode (LO) of tetragonal Te atoms [208]. With increasing temperature, this peak gradually weakened and disappeared beyond 200 K as shown in the inset of Figure 5.10(a). The reason behind the appearance of such longitudinal vibrational mode might be the transition from the semiconducting to the metallic state in the system below 200 K. At lower temperatures, charge carrier mobility enhances due to the reduced thermal scattering. Thus, strongly interacting surface electrons and bulk phonons suppress conventional spin plasmon modes at the Brillouin Zone boundary. And the collective charge carrier oscillation combined with a quasi-particle denoting intermingling electrons with atoms, formulates the plasmon-polaron interaction. As has been observed earlier, the broad metal-semiconductor transition from 200 K to 100 K is associated with the formation of plasmon-polaron (Figure 5.5(a)). This phenomenon is the probable reason behind the introduction of the distinct inconsistency at 150 K for all the Raman modes as displayed in the temperature-dependent surface colorplot (Figure 5.10(b)). In this temperature region, due to the formation of excess charge carriers (top inset of Figure 5.5(c)), the longitudinal vibration may take place by arising the infra-red active A^1 mode and disappears above 200 K. All the vibration modes were fitted with the Lorentzian line shape function as,

$$y = y_0 + \frac{2A}{\pi}\left(\frac{\omega}{4(\chi-\chi_c)^2+\omega^2}\right) \quad (5.5)$$

and deconvoluted to multiple peaks. Raman line shift corresponding to each vibrational mode (χ_c), full width half maxima (FWHM) (ω) and area under the curve (A) were evaluated from the fitted spectra at all temperature ranges. The evaluated Raman line frequency (χ_c) and FWHM (ω) were plotted with corresponding temperatures for all the phonon modes (Figure 5.8(b), 7(b), 8(a)). All the phonon modes show red-shift with enhancing temperature below 400 K. The red-shift of all vibrational modes is expected because at high temperature, the inter-planar spacing between the quintuple layer increases. Thus, it weakens the inter-planar bonds' strength, hence lowering the vibrational frequency of phonon modes resulting in the red-shift in the Raman line [206], [209].

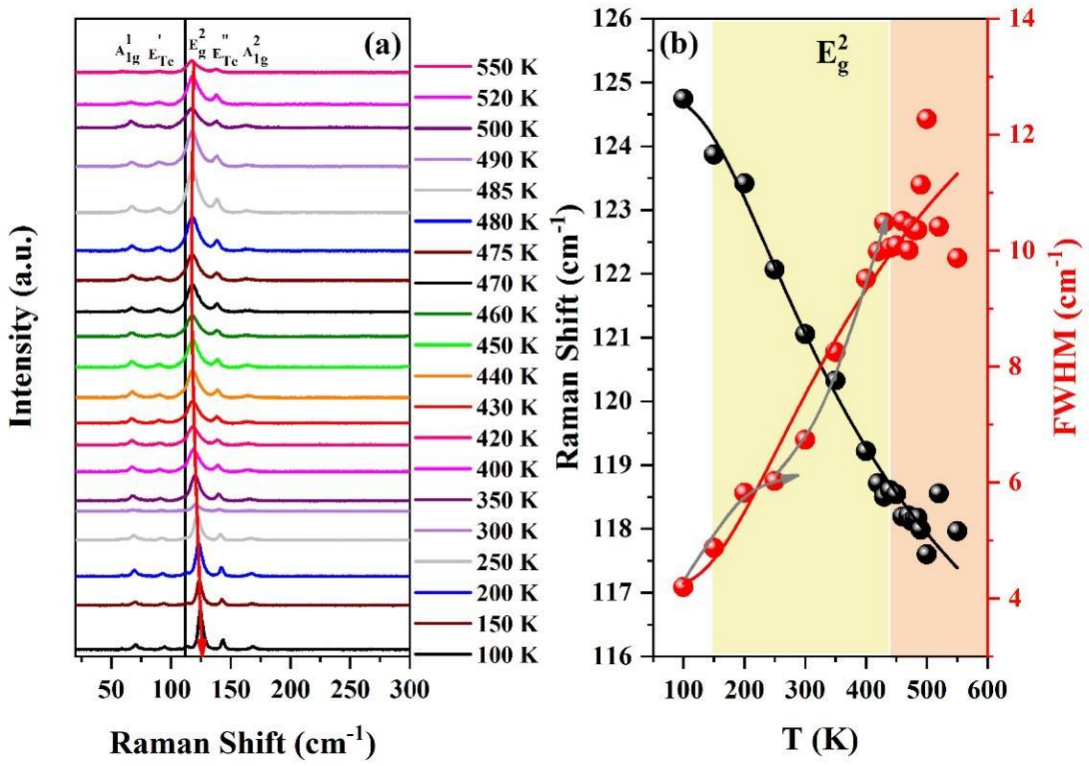

Figure 5.8: (a) Raman spectra contain all phonon modes from 100 K to 550 K temperature. (b) Raman line shift and line width plotted against temperature and fitted by AD model for E_g^2 phonon mode.

In Figure 5.8(a), the red curved line specifies the apparent shift in Raman frequency corresponding to E_g^2 mode. The peak is examined to be shifted towards lower wavenumbers (Figure 5.8(a)), which can be denoted as the red-shift. Detailed analysis on the red-shift of

Raman peaks and the theoretical determination of temperature coefficients initializes the investigation of thermal conductivity, thermal expansion and inter-layer coupling of the proposed material. The thermal expansion of the crystal and phonon modes on increasing temperature cause anharmonicity resulting in the temperature-dependent peak shifting of Raman active modes from 100 K to 400 K temperature range. From 450 K, the characteristic Raman mode E_g^2 shifts towards a higher wavenumber with raising the temperature. Interestingly, a local magnetic ordering between 465 K to 485 K has also been observed in Figure 5.7(d). A similar anomaly has been observed for all the phonon modes and is manifested with a red curved line in Figure 5.9(a). Generally, in the absence of any additional perturbation like electron-phonon/spin-phonon coupling, magnetostriction, structural transition, etc., the temperature variation of the Raman shift follows the anharmonic equation as given by [91], [210],

$$\chi_{c_{anh}} = \chi_{c_0} - C\left(1 + \frac{2}{e^{\frac{\hbar\omega_0}{2K_BT}} - 1}\right) \tag{5.6}$$

Whereas the line width (FWHM) can be fitted with the equation [91], [210],

$$\omega_{anh} = \omega'_0 + C\left(1 + \frac{2}{e^{\frac{\hbar\omega_0}{2K_BT}} - 1}\right) \tag{5.7}$$

A model with anharmonic phonons decays [211], [212] (AD) into acoustic phonons from the optical phonons with the same frequencies and opposite momenta and derives those two equations. $\chi_{c_{anh}}$ and ω_{anh} are the modulated χ_c and ω (FWHM) and χ_{c_0} and ω'_0 as the bare phonon frequency and linewidth of a particular phonon, respectively. C comprises the transition matrix element and the two-phonon density of states of the anharmonic decay. The fitted data accordant to the anharmonic decay model is shown as black and red lines in Figure 5.8(b) & Figure 5.9(b-e). The anharmonic fits are compatible with the data points for the characteristic E_g^2 mode (Figure 5.8(b)). The linewidth is showing a very weak

deviation from the AD model below 200 K, which can be seen in Figure 5.8(b). As described earlier, there is a metal to semiconductor transition around 150 K, suggesting the possibility of electron-phonon coupling in the system under investigation. A substantial deviation from AD model is observed above 450 K in Figure 5.8(b). This aberration from anharmonic behavior by displaying additional distinct anomalous softening above 450 K might occur due to the spin-phonon coupling. Such remarkable anomalous softening of vibrational modes is related to the inflection in the lattice vibrations due to a specific local magnetic ordering around 475 K in our system. Remarkably, the deviations of the data points are observed at both 150 K and 450 K temperatures for every individual Raman mode (Figure 5.9(b-e)). Also, a clear deviation in intensity and Raman lines is observed above 425 K in the 3-D contour plot as shown in Figure 5.10(b). The inconsistent behavior of Raman lines starting at 425 K towards higher temperature signifies that the electron spins are interacting with the phonons, quanta of lattice vibration in the system. The deviation of the wavenumber from the minima reaches the utmost beyond 475 K. This is consistent with the local ordering temperature confirmed by the magneto-transport properties. Thus, at around 475 K, due to the local spin alignment, the spin-phonon interaction strengthens following the deviation from the AD model. The fitting parameters evaluated from the AD model for all the phonon modes have a certain dependency on the Raman line shift as shown in Figure 5.11. χ_{c_0}value enhances with Raman line shift and the transition matrix element C decreases with increasing wavenumber till E_g^2 phonon mode showing the minima and enhances again for E"(Te) and A_{1g}^2 modes. The C value is similar for both E'(Te) and E"(Te) modes. This is clear evidence of sensing a similar kind of vibration (LO) corresponding to these two modes. Again, for both A_{1g}^1 andA_{1g}^2 Raman modes (TO) enhancement of the C value represents the similar phonon vibration in the confined system. This is noteworthy to observe that the lower wavenumber modes attribute weak deviations from the AD model.

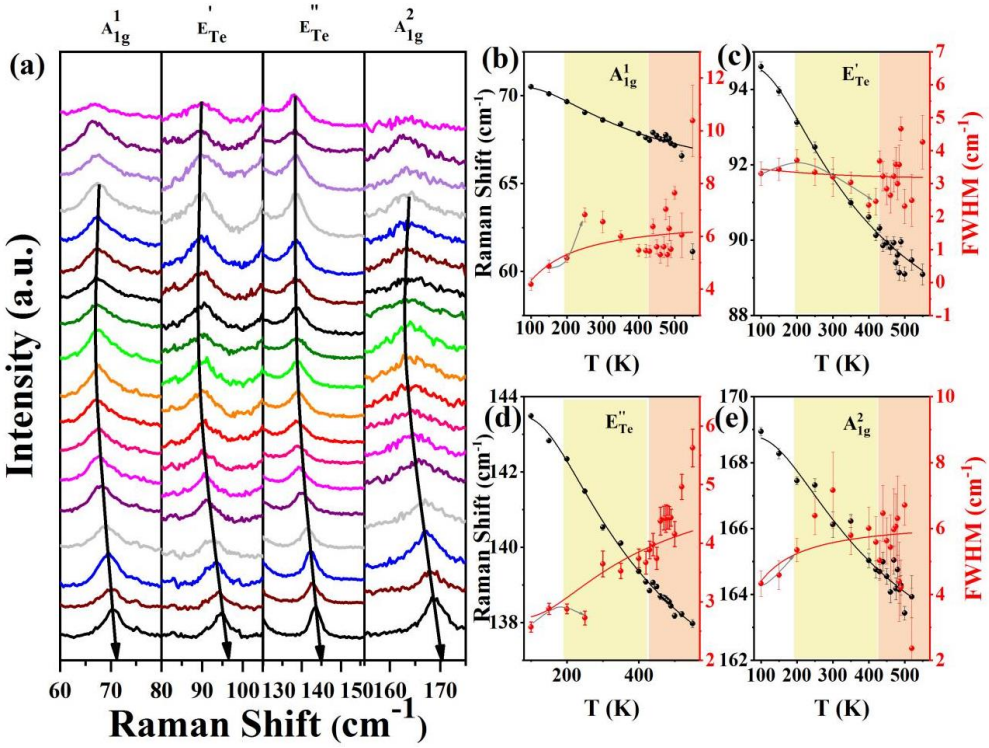

Figure 5.9: (a) Raman shifts for A_{1g}^1, A_{1g}^2, E'(Te) and E''(Te) vibrational modes. Peak center and FWHM plot with temperature for (b) A_{1g}^1, (c) A_{1g}^2, (d) E'(Te) and (e) E''(Te) phonon modes.

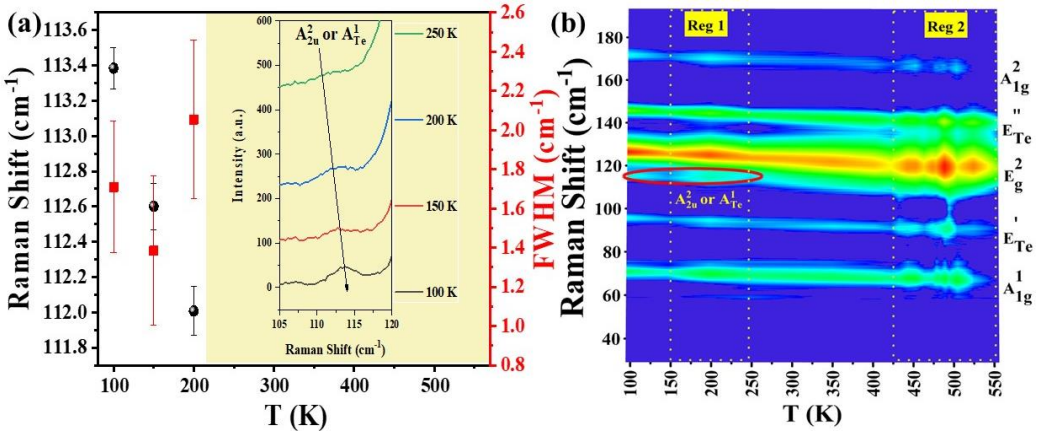

Figure 5.10: (a) Peak center and FWHM plot with temperature for A_{2u}^2 mode. Inset shows the Raman line shift at different temperatures for A_{2u}^2 mode. (b) Three-dimensional colormap of the temperature-dependent Raman spectra denoting all the Raman active modes.

But the higher energy modes diverge more from the anharmonicity (Figure 5.10(b-e)). This suggests that the nonconformity is curtailing due to the enlarged electronic surface contributions of the prepared film at lower temperatures. Hence, this phenomenon supports the enhanced electron density of the system near the Fermi surface.

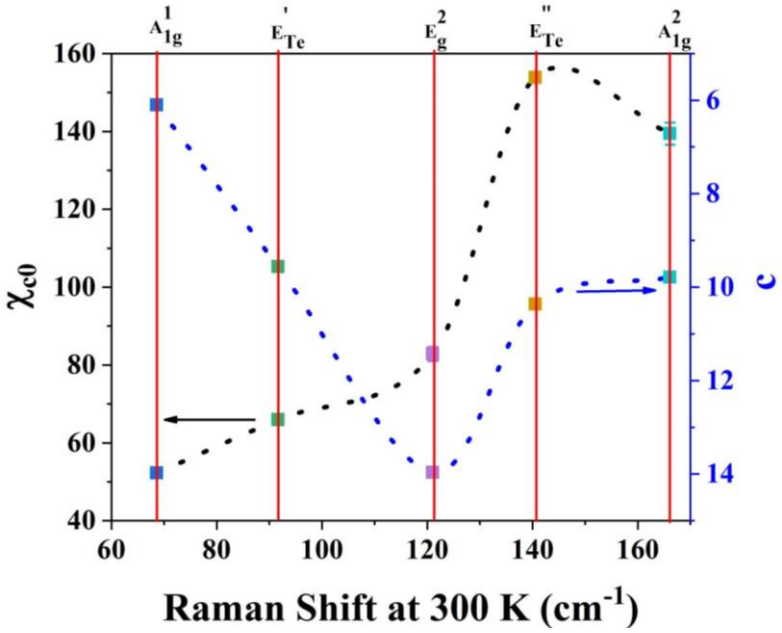

Figure 5.11: The dependency of AD fitting parameters χ_{c_0} and c on the Raman line shift.

5.4 Conclusion

The heterostructure manifesting two different chalcogenide systems prepared using the PLD technique demonstrated the reduced crystallite size as 11.81 nm and the grain size was calculated in the order of 300 to 400 nm. The structure was evidenced to be grown along the c-axis exhibiting pyramid-shaped characteristic triangular islands under electron microscopy. From the evolution of resistivity with temperature, a metal-semiconductor transition was examined below 150 K. This transition was consistent with the enhanced charge carrier density attributed to the transverse resistivity. This transition was further confirmed to be initiated by electron-phonon interaction, which was probed by investigating the Raman shift with varying temperatures. The thermal variation of Magnetization exhibits weak parallel and anti-parallel spin alignments which were inveterate at different temperature ranges. The anti-parallel spin alignment was demonstrated at a very low temperature ($< T_1$), which is consistent with the well-established Kondo model fitted in the resistance data below 15 K temperature and a Kondo transition

has been demonstrated at ~5.4 K. Presence of FeSe at the inter-layer propinquity accomplishes the magnetic impurity in TI layer diminishing the conductivity at low temperature. Magnetization value drops suddenly adjacent to 475 K, signifying some local charge ordering at the vicinity of interfacial domains dominating over intrinsic bulk effect at that temperature range. More interestingly, the study of lattice vibrational phonon modes also shows certain anomaly above 450 K. This, local magnetic ordering evidencing the anomalous behavior in Raman shifts demonstrating the signature of spin-phonon coupling driven by charge ordering at the edges of the particular 75.3 nm thick heterostructure. Thus, the proximity-induced local charge orientation at the interfaces of the tetragonal FeSe and rhombohedral Sb_2Te_3 is modified enormously depending on the confinement of the sandwiched structure. Such dimensional sensitivity to Magnetization competes with the recent development of the layered materials featuring such FM/TI/FM heterostructure suitable for spintronics application.